ARTICLE Open Access

Optically programmable dual-band perovskite single-pixel detector for color image encryption

Ai Fu[1], Zhi-Hong Zhang[1,2], Jiahao Xiong[1], Xuan Zhang[1], Zhiyuan Ye[3], Jun Xiong[3], Zhi-Peng Wei[2], Shuang Zhang[4,5]✉, Shuang-Peng Wang[1]✉ and Hong-Chao Liu[1]✉

Abstract

The rapid evolution of eavesdropping technologies has encouraged regular updates and improvement of encryption systems. Developing a detector-dependent optical encryption scheme to tightly connect the decryption and imaging processes offers great potential to prevent eavesdropping. By designing an optically programmable dual-band photodetector, a color image encryption scheme where the photodetector functions as both a detector and a critical decryption key is demonstrated here. The distinctive optically programmable property of the photodetector enables the manipulation of its long-wavelength sensitivity via short-wavelength photonic stimulation, leading to different imaging outputs between single-pixel imaging and point-scan imaging, which therefore demonstrates a capability to decrypt information hidden in color images. This detector-dependent decryption method can effectively prevent potential information leaks when other detectors are used as eavesdropping devices. Our encryption paradigm opens new avenues for color image encryption using photodetectors, enhancing encryption security by introducing a device-based dimension.

Introduction

Traditional digital cryptography techniques concentrate on developing advanced cryptographic algorithms to ensure information security, with challenges of long latency and high computing demands[1,2]. In contrast, optical encryption[3] attracts increasing attention for its low power consumption, high-speed parallel processing, and easy-control of multiple degrees of freedom (DoFs) of light (e.g., amplitude, wavelength, phase, and polarization)[4,5], thus providing a fertile platform to achieve diverse efficient and secure encryption schemes[6–8]. For instance, one DoFs-dependent paradigm involves encoding a number of images into a millimeter-sized metasurface. These encrypted holographic images can be retrieved by using an incident light with correct DoFs, where the DoFs of light act as keys. Typically, a camera is integrated in the optical link to assist in observing and recording the decrypted optical images[9,10]. However, while such portable and promising schemes offer significant potential, they face a critical vulnerability to information leakage - not in the optical front-end used for metasurface-enabled encoding, but in the back-end used for optical detection. With the rapid advancement of various non-invasive imaging and sensing technologies, any optical mode transmitted through public media, including free space and optical fibers, is at risk of potential eavesdropping, owing to the fact that any escaping scattered or diffused light may lead to information leakage[11,12]. Therefore, there is an urgent need to closely integrate the decryption and imaging processes to address the vulnerability prevalent in the current top-heavy encryption schemes. Integrating optical encoding/decoding function at the detector end would be a reliable strategy, this kind of detector-dependent optical cryptography ensures that secret information is only visible to the specially designed detectors, thereby enhancing robustness of optical encryption.

Traditional optical imaging and encryption rely on focal-plane array photodetectors, such as complementary

Correspondence: Shuang Zhang (shuzhang@hku.hk) or
Shuang-Peng Wang (spwang@um.edu.mo) or
Hong-Chao Liu (hcliu@um.edu.mo)
[1]Institute of Applied Physics and Materials Engineering, University of Macau, Taipa, Macao SAR, China
[2]State Key Laboratory of High Power Semiconductor Lasers, Changchun University of Science and Technology, Changchun, China
Full list of author information is available at the end of the article
These authors contributed equally: Ai Fu, Zhi-Hong Zhang

metal-oxide-semiconductor (CMOS) sensors and charge-coupled devices (CCDs)[13]. The direct imaging method enabled by array photodetectors can potentially lead to another type of information leakage, as attackers may exploit vulnerabilities in photodetectors to access the captured images[14]. Consequently, these array photodetectors, which serve as the eyes of optical encryption schemes, are increasingly facing significant information security challenges. Recently, single-pixel detectors (SPDs) have been employed to obtain high-resolution images, known as single-pixel imaging (SPI)[15–18]. As an indirect imaging method, SPI can effectively strengthen information security against potential eavesdropping by encoding the objects' spatial information into indistinguishable one-dimensional intensity signals[9,19]. Meanwhile, relying on SPDs, SPI also offers the advantages of low cost and high stability, avoiding the challenges of large-area integration for array photodetectors[20,21]. However, color image encryption, which enhances the security of information secreting by offering one more information dimension than grayscale[22,23], is inapplicable to conventional filter-free silicon-based SPD (Si-SPD) due to lack of adjustable wavelength response[24]. In contrast, halide perovskites, with significant advantages in flexibly tunable bandgaps, superior photoconductivity, and low-cost solution processing[25–27], emerge as a promising option for color sensing[28,29]. For instance, a perovskite-based single-pixel camera has been demonstrated to achieve 256 × 256 pixels color imaging[30]; a double-layer integrated perovskite SPD has been reported to show high performance in dual-color imaging recognition[31]. While these results demonstrate the superiority of perovskite-based detectors over conventional detectors (e.g., silicon photodetectors) in color discrimination[31,32], these benefits have not yet translated into unique applications in imaging technologies, particularly in optical information encryption-decryption.

This article reports development of a color image encryption scheme that seamlessly integrates the imaging and decryption processes by designing an optically programmable dual-band perovskite photodetector which functions as both a detector and a critical decryption key. This lateral perovskite microwire heterostructure single-pixel-detector (PMH-SPD) is composed of $MAPbBr_3$-$MAPbBr_{3-x}I_x$ microwire heterostructure arrays, wherein the unexcited low-conductivity $MAPbBr_3$ acts as a barrier for the carriers generated in $MAPbBr_{3-x}I_x$. Thus the long-wave response of $MAPbBr_{3-x}I_x$ can be modulated by the excitation state of $MAPbBr_3$, facilitating the programmable manipulation of long-wavelength sensitivity via short-wavelength photonic stimulation. By utilizing Hadamard and point-scan-like patterns in SPI modality, these modulatable photoelectric characteristics enable the detector to decrypt the hidden information ("OK") within the color image under complex disturbances (including color confusion and scattering medium), which would be

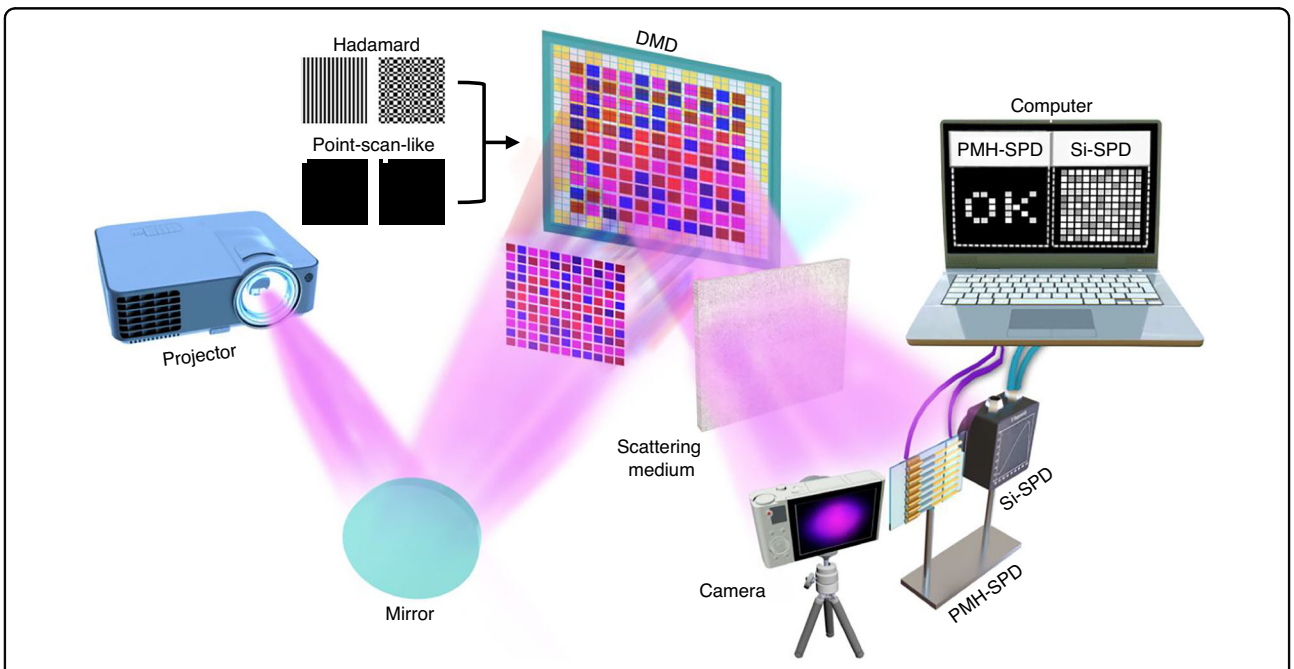

Fig. 1 The color image encryption system based on the PMH-SPD. Comparison of the decryption results between the commercial camera, PMH-SPD and Si-SPD in the presence of a scattering medium used Hadamard and Point-scan-like patterns for an encrypted color image projected by a projector. Correct information ("OK") is hidden in the color image (mixed color consisting of red and blue, excluding green), and can be decrypted by the PMH-SPD, but not the commercial camera or the Si-SPD. DMD digital micromirror device

impossible for decryption by using a commercial camera or a conventional Si-SPD (Fig. 1). With different imaging outputs between single-pixel imaging and point-scan imaging, this detector gives unique color discrimination capability, which opens a new door for detector-based color image encryption.

Results

Fabrication and characterization of the PMH-SPD

The lateral PMH-SPD is composed of the $MAPbBr_3$-$MAPbBr_{3-x}I_x$ heterostructure and electrodes at both ends, as shown in Fig. 2a. The $MAPbBr_3$ microwire arrays were first synthesized by a solution preparation method[32,33], with one end anchored on the ITO electrode (~150 nm thickness). The microwire arrays exhibit large-area uniformity, with each microwire having a width of ~1.35 μm and a height of about 600 nm (Supplementary Fig. S1). Subsequently, the glass-side of the $MAPbBr_3$ microwire arrays were converted into $MAPbBr_{3-x}I_x$ through a regioselective anion exchange method[34,35], thereby forming the lateral $MAPbBr_3$-$MAPbBr_{3-x}I_x$ heterostructure (Supplementary Fig. S2). The microscopic images of the heterostructure (Fig. 2b) show that after the anion exchange, the $MAPbBr_{3-x}I_x$ side turns from yellow to black and no longer emits green luminescence when excited. A clear boundary separates $MAPbBr_3$ and $MAPbBr_{3-x}I_x$, and the gradient conversion near the boundary indicates the seamless lateral structure. Crystal structure and spectral analyses (Supplementary Fig. S3) further verify the successful fabrication of the lateral $MAPbBr_3$-$MAPbBr_{3-x}I_x$ heterostructure. Finally, an Au electrode (~100 nm thickness) was deposited on the $MAPbBr_{3-x}I_x$ arrays side via thermal evaporation to complete the fabrication of PMH-SPD (Supplementary Fig. S2). This multi-microwire integration helps to eliminate device disparity and improve photoelectric performance.

Photoelectric characteristics of the PMH-SPD

The PMH-SPD has a 400 μm channel, wherein $MAPbBr_3$ responds to visible wavelengths below 560 nm and $MAPbBr_{3-x}I_x$ to wavelengths below 720 nm (Supplementary Fig. S4). The broader detection range of $MAPbBr_{3-x}I_x$ endows the PMH-SPD with unique photoresponse characteristics. As evidenced by the intensity-dependent photocurrent of the PMH-SPD (Fig. 2c), the detector exhibits superior sensitivity to 450 nm radiation compared to 650 nm excitation. Under 5.0 V bias, with a dark current of 1.85×10^{-11} A, the PMH-SPD demonstrates high sensitivity to 450 nm input, achieving an

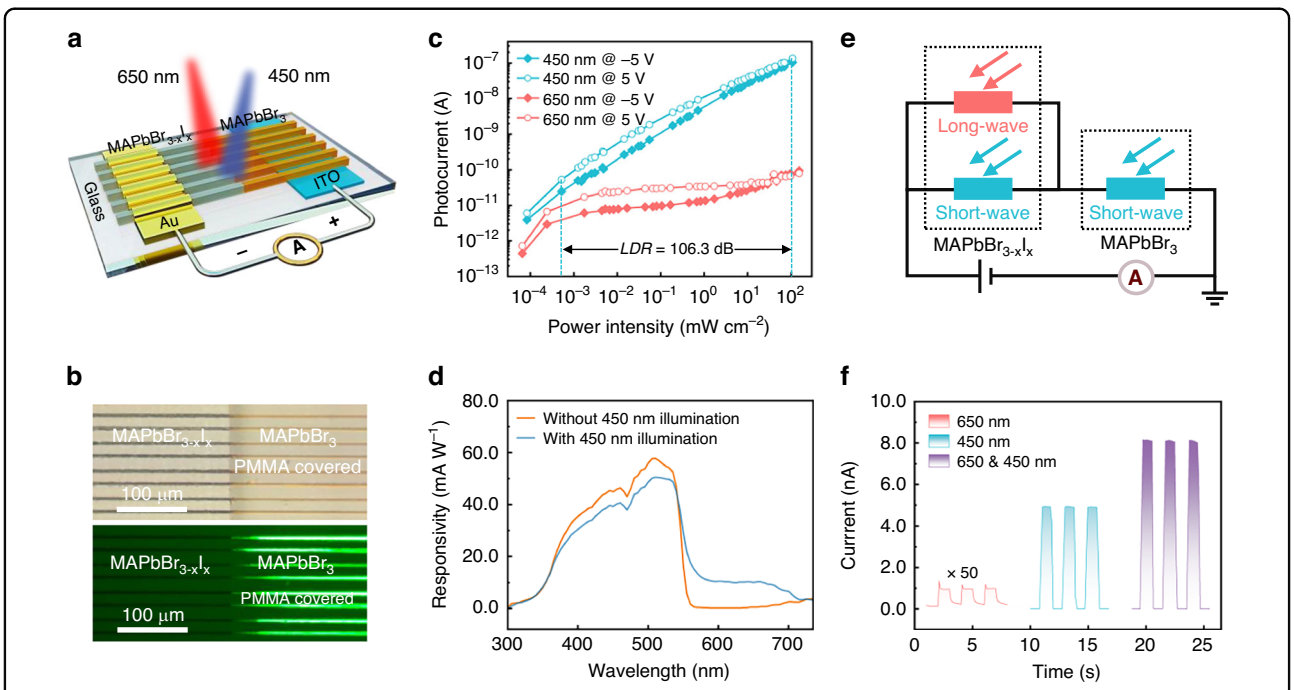

Fig. 2 Photoelectric characteristics of the PMH-SPD. a Diagram of the PMH-SPD. **b** Optical microscope and Fluorescent microscope images of the lateral $MAPbBr_3$-$MAPbBr_{3-x}I_x$ heterostructure. **c** Photocurrent of the PMH-SPD under 650 nm and 450 nm illumination versus laser intensity at bias of ±5.0 V, demonstrating a wide linear dynamic range (*LDR*) of 106.3 dB for 450 nm signal. **d** The spectral responsivity without and with 450 nm illumination (15 μW cm^{-2}, approximately equal to the intensity used in the response spectrometer). **e** Equivalent circuit of the PMH-SPD under negative bias; the blue photoconductors respond to short wavelengths (below 560 nm), and the red photoconductor responds to long wavelengths (above 560 nm). **f** The photocurrent under 650 nm (amplified 50-fold), 450 nm, and (650 & 450) nm illumination, with all laser intensities set to 0.72 mW cm^{-2}

exceptional on-off ratio (I_{ph}/I_{dark}) exceeding 10^4, while the 650 nm excitation yields a significantly lower maximum on-off ratio of ~11. This remarkable disparity leads to a three-order-of-magnitude photocurrent differentiation ($I_{450\ nm}/I_{650\ nm} = 10^3$) at the same power densities. Systematic characterization of the device's photoelectric performance, including responsivity (*R*), specific detectivity (*D**), and external quantum efficiency (*EQE*), quantitatively confirms the pronounced wavelength-dependent response disparity between 450 nm and 650 nm inputs (Supplementary Fig. S5). Notably, the performance gap exhibits progressive enhancement with increasing incident power intensity (Supplementary Fig. S6). The response spectrum graphically illustrates this tremendous difference (Fig. 2d yellow line), which is similar to the spectral response of $MAPbBr_3$ (Supplementary Fig. S4a). Interestingly, under 450 nm illumination, a significant enhancement in responsivity is observed at long wavelengths (550–720 nm), accompanied by a slight reduction at short wavelengths (350–550 nm) (Fig. 2d blue line). The diminished responsivity at shorter wavelengths further demonstrates the inverse correlation between responsivity and power intensity (Supplementary Fig. S5a). More importantly, the enhanced long-wave responsivity indicates that 450 nm illumination effectively improves the PMH-SPD's long-wavelength response. This phenomenon essentially originates from the photoconductive nature of perovskites. Specifically, while both $MAPbBr_3$ and $MAPbBr_{3-x}I_x$ are responsive to 450 nm radiation (Supplementary Fig. S4), only $MAPbBr_{3-x}I_x$ demonstrates sensitivity to longer wavelengths (550–720 nm). This implies that carriers generated in $MAPbBr_{3-x}I_x$ by 650 nm are blocked by the unexcited $MAPbBr_3$ part, preventing their effective transport across the entire device channel, which results in low responsivity. However, under 450 nm illumination, $MAPbBr_3$ becomes conductive, facilitating the transport of carriers generated in $MAPbBr_{3-x}I_x$ and thereby enhancing the long-wavelength responsivity. These observations collectively indicate that the PMH-SPD operates on the photoconductor principle, and the underlying working mechanism is further corroborated through comparative experiments (Supplementary Fig. S8).

This unique response characteristic endows the PMH-SPD with a specific logic functionality: 450 nm illumination can significantly enhance the on/off ratio from a 650 nm signal. Figure 2e illustrates the equivalent circuit diagram of the photoconductive device. Under 650 nm illumination, only the red photoconductor is photoexcited, leaving the circuit in the OFF state. Under 450 nm illumination, both blue photoconductors are photoexcited, activating the circuit. When exposed to dual-chromatic illumination (650 & 450 nm), all three photoconductors are photoexcited, turning the circuit on with higher total conductivity compared to illumination with 450 nm alone. The current variations under different photonic stimulations (Fig. 2f) demonstrate that the PMH-SPD possesses an optically programmable property, enabling the modulation of its long-wavelength response by short-wavelength stimulation. These optically modulated current variations can be controllably regulated by adjusting illumination intensity and bias voltage: Increased illumination promotes a stronger modulation effect, while a greater bias voltage linearly amplifies the current variation (Supplementary Figs. S10, S11). Specifically, the 650 nm photocurrent can be enhanced by up to 10^3 times through 450 nm illumination. Furthermore, the device exhibits submillisecond rise and decay times (~350 μs and ~370 μs, respectively, Supplementary Table S1), a 3 dB bandwidth (8.4 kHz), and exceptional long-time on/off stability (with only a 1.61% variation in the amplitude of photocurrent over 10^3 s) (Supplementary Fig. S12). These characteristics establish the PMH-SPD as an ideal candidate for color imaging applications. Notably, the PMH-SPD, with its programmable sensitivity, is able to generate distinct imaging outcomes, a capability unattainable by conventional silicon-based detectors due to their nonadjustable sensitivity. Comparative analyses of recent dual-band photodetectors (Supplementary Table S2) reveal that dual-band detection is primarily achieved through voltage modulation or material and structural design, with optically programmable modulation remaining relatively scarce[36–38]. This optically programmable responsivity offers the potential to reveal hidden information invisible to other detectors, thereby unlocking promising applications in color image encryption.

Color image encryption based on the PMH-SPD

Leveraging the optically programmable characteristic of PMH-SPD, its application in the field of SPI-based image encryption was explored. The imaging system is displayed in Fig. 1. In this setup, a color target image generated by a projector was first modulated by a digital micromirror device (DMD). Subsequently, the modulated light passed through a scattering medium and was finally detected by the detectors. Here, a long-channel PMH-SPD (1600 μm channel) was employed to detect the weak light (about 1–100 $\mu W\ cm^{-2}$) due to its better optical modulation capability (Supplementary Fig. S14). Meanwhile, a Si-SPD was employed as a control for comparative analysis. The target image can be reconstructed through a differential correlation imaging algorithm[39], which correlates the modulated intensity signals recorded by the detectors with the corresponding modulated Hadamard patterns[40] on DMD.

Some typical 32-order Hadamard patterns are displayed in Fig. 3ai (see also Section 3.1 of the Supplementary Information). Since SPD operates using bucket detection,

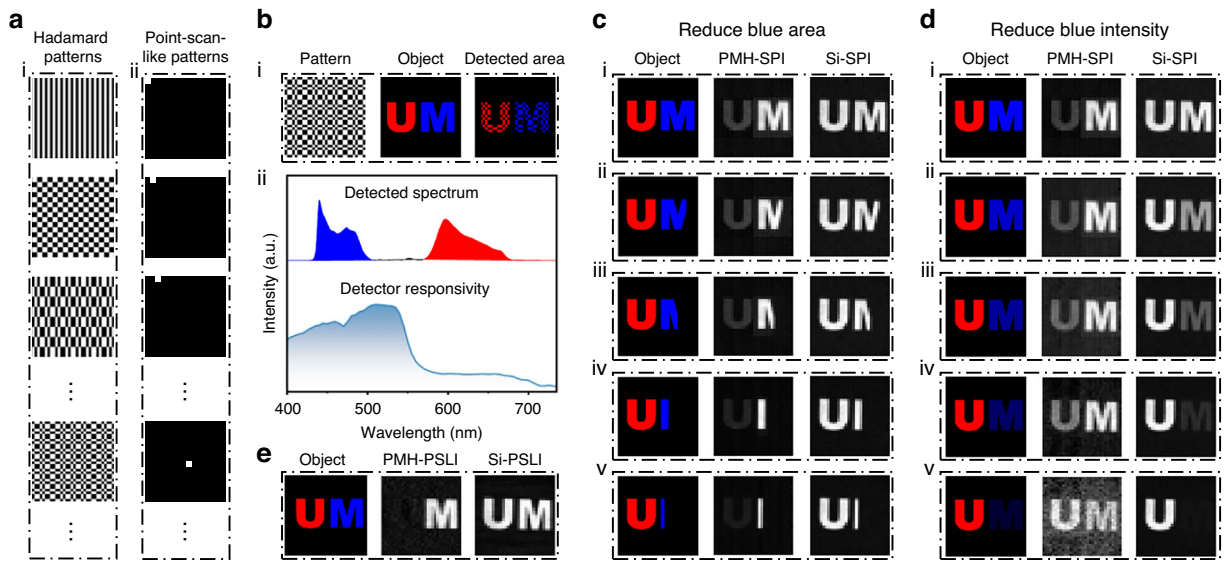

Fig. 3 Imaging results of the PMH-SPD for red-blue objects by using SPI and PSLI. a Typical 32-order (i) Hadamard patterns, and (ii) Point-scan-like patterns (the bright points are enlarged by 4 times for better demonstration). **b** The PMH-SPD's (i) detection area corresponding to the object image, and (ii) detected spectrum for one single Hadamard pattern (obtained via a spectrometer); the spectral responsivity of the PMH-SPD under 450 nm illumination is shown for comparison. Comparison of the SPI results between the PMH-SPD and Si-SPD for the red-blue objects with **c** different blue areas and **d** different blue intensities (the pixel intensities (R, G, B) of blue "M" in i-v are (0, 0, 255), (0, 0, 204), (0, 0, 153), (0, 0, 102), and (0, 0, 51), respectively). **e** Comparison of the PSLI results between the PMH-SPD and Si-SPD for the red-blue object

both red and blue signals from different areas will be recorded simultaneously when the object is modulated by a Hadamard pattern (Fig. 3bi), which can be confirmed by a spectrometer-acquired spectrum (Fig. 3bii). This configuration enables the PMH-SPD to reliably detect blue light while utilizing this blue illumination to optically modulate the response in the red spectral region.

Employing "UM" as a target image, as illustrated in Fig. 3ci, the PMH-SPD demonstrates a high-contrast image for the blue "M", but a reduced contrast for the red "U" element. This different imaging performance originates from the device's wavelength-dependent responses to the projected blue and red light, as quantitatively characterized in Supplementary Fig. S15, which is consistent with the spectral response in Fig. 2d. Different from the Si-SPD behavior, the experimental observation in Fig. 3ci–v reveal a progressive vanishing of the red "U" from the reconstructed images when maintaining constant red illumination to "U" while incrementally reducing the blue "M" exposure area. This phenomenon arises from the PMH-SPD's unique optoelectronic coupling mechanism: decreasing blue photon flux proportionally reduces the device's red-light responsivity through its photosensitive heterostructure modulation characteristics (Fig. 2d). The resultant nonlinear suppression of photocurrent generation ultimately disrupts the red element reconstruction. In contrast, the Si-SPD preserves the characteristics of conventional SPI, demonstrating similar imaging contrast for both red and blue regions. Furthermore, under fixed red illumination ("U") while reducing the intensity of the blue "M" (Fig. 3di–v) gradually, the reconstructed red "U" from the PMH-SPD gradually becomes clearer, and finally reaching similar intensity level as the blue "M" at extremely low blue intensity, even undetectable to human visual. However, this change also introduces considerable background noise in the reconstructed images, similar to the low-contrast image for the red object in Supplementary Fig. S15c. This is because reducing the intensity of the blue "M" simultaneously decreases the detected blue intensity and increases the red-to-blue contrast in the target image. When the blue intensity decreases, its modulation capacity gradually diminishes. In addition, as illustrated in Fig. 2d, the PMH-SPD's significantly different responses to red and blue light enable its potential application in identifying objects with high red-blue contrast (bright-red against dark-blue). Consequently, the increasing red-blue contrast leads to a clearer "U". In comparison, the reconstructed images of the Si-SPD remain consistently in line with the target images. In addition, when reducing the intensity of the red "U" or simultaneously reducing the intensities of the red "U" and blue "M" (Supplementary Fig. S16), both the PMH-SPD and Si-SPD exhibit similar changes in response to the target image, and the "U" reconstructed by the PMH-SPD disappears faster due to its weaker red-light responsivity. To summarize, the SPI configuration allows

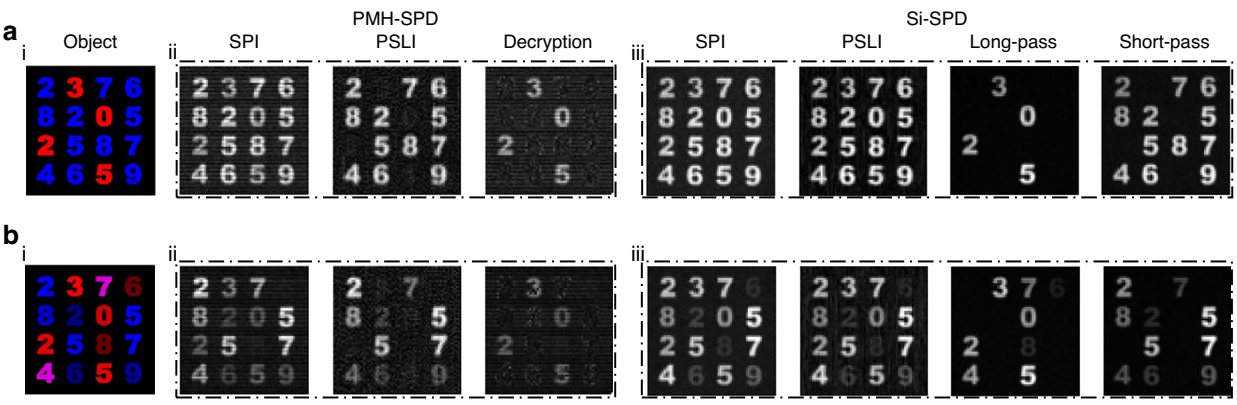

Fig. 4 Decryption results for different color object images with the PMH-SPD and Si-SPD applying both SPI and PSLI methods. (i) The object images, (ii) SPI, PSLI, and decrypted results of the PMH-SPD, (iii) SPI and PSLI results of the Si-SPD, as well as SPI results of the Si-SPD equipped with long- and short-pass filters of the encrypted object **a** with same red and blue intensity, **b** with various composite red-blue colors and red-blue intensities

the detected blue light to modulate the PMH-SPD's red-light responsivity, thereby enabling a distinctive optically programmable imaging capability such that the detected blue light helps to reconstruct red objects, which contributes to achieving a richer variety of imaging outcomes.

In the traditional point-scan-like imaging (PSLI) method, the SPD is used to detect just one point of the object at a time[41,42]. Since both SPI and PSLI reconstruct the amplitude information of the object, the Si-SPD produces similar imaging results by using SPI and PSLI (Fig. 3e). However, for the PMH-SPD, which features optically programmable responsivity, SPI and PSLI can yield dramatically different reconstructed images because PSLI does not allow interaction between different colors (Supplementary Fig. S18). Thus, SPI based on PMH-SPD facilitates effective information extraction from dual-color images.

Figure 4ai illustrates another example of encryption in which the information to be hidden, "3025" is shown in red, while the other blue numbers act as the controlling units. The pixel intensities of these numbers are displayed in Supplementary Fig. S19a. The image was projected onto the DMD and interacted with the 64-order Hadamard and Point-scan-like patterns shown on the DMD. The PMH-SPD and Si-SPD are employed to capture the reflected light intensity through the scattering medium to reconstruct images, respectively. As shown in Fig. 4aii, with the PMH-SPD, the full image (ciphertext) can be successfully reconstructed by applying SPI, while PSLI can only reconstruct the blue numbers. Therefore, the hidden information ("3025") can be revealed by a simple subtraction between the SPI and PSLI results (Supplementary Fig. S20). In contrast, a commercial camera cannot capture any information (Fig. 1 and Supplementary Fig. S22a) through the scattering medium. Meanwhile, the conventional Si-SPD obtains the same results using SPI and PSLI (Fig. 4aiii), but the information can be extracted when optical filters with predefined wavelengths are employed. However, the filter-assisted method becomes ineffective against disturbances involving composite or identical colors.

To demonstrate the PMH-SPD's exceptional performance in information extraction, the target image was modified in terms of brightness and color (Fig. 4bi), with pixel intensities displayed in Supplementary Fig. S19b. The modification incorporates three types of elements: (1) weak-blue numbers (such as "2", "6" and "9"), (2) numbers with composite red-blue color (such as "7" and "4"), and (3) weak-red numbers (such as "6" and "8"). The modified object features a non-uniform brightness distribution and contains disturbances involving composite and identical colors. As shown in Fig. 4bii, the SPI using PMH-SPD reconstructs all numbers except the weak-red numbers ("6" and "8"), while the PSLI fails to resolve both the weak-red numbers ("6" and "8") and the correct information ("3025"). Nonetheless, the hidden information can still be obtained using the subtraction method. Importantly, the inclusion of composite and identical color disturbances ensures that hidden information remains secure against detection using a Si-SPD (Fig. 4biii), as well as a commercial camera (Supplementary Fig. S22b). As shown in Fig. 4biii, even if eavesdroppers attempt to employ long-pass or short-pass optical filters and adopt the image thresholding method[43] along with efforts to eliminate composite color disturbances captured by a Si-SPD, the non-uniform brightness distribution and identical color disturbances remain effective in thwarting such interception attempts (Supplementary Fig. S23). These adjustments have proven to be highly effective in maintaining encryption safety, enabling the PMH-SPD to offer

significant advantages over a Si-SPD, which is precisely confirmed by the quantitative evaluation of correlation coefficient (Supplementary Fig. S24). Hence, the optically programmable sensitivity of the PMH-SPD enables its unique abilities to decrypt color information from complex disturbances, demonstrating its functionalities as both a detector and a critical decryption key in a high-security detector-dependent color image encryption system.

Discussion

Compared to conventional optical color image encryption that employs diverse algorithms to independently encrypt the red, green, and blue components of target images[44,45], the proposed detector-dependent encryption scheme offers several advantages. It utilizes a compact, filter-free detector to decrypt information hidden in color images, effectively preventing potential information leakage by tightly integrating the decryption and imaging processes. Unlike in-sensor cryptography which makes use of a photodetector array to encrypt the target grayscale images during the imaging process (i.e. integration of the imaging and encryption processes)[14], the present method focuses on utilizing an SPD to decrypt the pre-encrypted color images (i.e. integration of decryption and imaging processes) to prevent monitoring by other detectors. The present method ensures that the information transmitted along the light path is securely encrypted within color images, making it inaccessible to other detectors. In comparison to the vertical perovskite photodetectors designed for color sensing[31,46], which are not applicable to imaging decryption, the PMH-SPD here achieves color sensing with a lateral device structure, which does not require complex fabrication or the consideration of damages between different materials during fabrication. Furthermore, benefiting from the tunable bandgaps[25] of perovskites as well as the strategies of narrow-band detection[47–49], the detected wavelengths of the PMH-SPD are adjustable, thus making it possible to customize the tunable narrowband PMH-SPD. By precisely designing the detection wavelength as an additional security key, the security of above color encryption method can be further improved. Notably, the present method employs perovskite, a photoconductive semiconductor, to construct an optically programmable photodetector. This pioneering method, fundamentally governed by photoconductive principles, represents a universal modulation strategy, which could be extendible to alternative structures or material morphologies (Supplementary Fig. S25). This detector-level architecture reveals the significant imaging difference between an SPI and a PSLI, challenging the conventional assumption that both modalities yield equivalent imaging outputs.

In conclusion, an optically programmable dual-band PMH-SPD has been developed and its potential for secure and efficient color image encryption has been demonstrated through tightly integrated decryption and imaging processes. The optically programmable sensitivity results in distinct imaging outcomes between SPI and PSLI, enabling decryption of information concealed in color images. This decryption method improves upon the commercial camera and conventional Si-SPD, effectively preventing potential information leakage. Within this detector-dependent encryption framework, the PMH-SPD functions as both a detector and a critical decryption key, compatible with most existing optical encryption systems, such as metasurface- and SPI-based encryption[9,10]. The approach extends encryption security into a device-based dimension, enhancing the robustness of optical encryption strategies.

Materials and methods

Materials

Methylammonium bromide (MABr, 99.99%) and lead bromide ($PbBr_2$, 99.99%) were purchased from Xi'an Yuri Solar Co., Ltd. N,N-dimethylformamide (DMF, anhydrous, 99.9%), and dimethyl sulfoxide (DMSO, anhydrous, 99.9%) were purchased from Aladdin Chemistry Co., Ltd. Poly methyl methacrylate (PMMA) and Hydroiodic acid (HI, 55.0-58.0%) were purchased from Macklin Reagent Co., Ltd. Chlorobenzene (CB, 99.8%) was purchased from Thermo Fisher Scientific Inc. Silicon elastomer (PDMS, SYLGARD-184) and curing agent were purchased from Dow Inc. Silica gel was purchased from Sinopharm Chemical Reagent Co., Ltd. Unless otherwise stated, the reagents and solvents were used directly without any purification.

Synthesis of $MAPbBr_3$-$MAPbBr_{3-x}I_x$ microwire heterostructure arrays

Materials and precursor preparation

MABr and $PbBr_2$ were mixed with a molar ratio of 1:1 and added into DMF and DMSO in a volume ratio of 4:1 to form a 0.2 M precursor solution, then stirred one night at 60 °C to get a transparent and clear solution. 1.0 g PMMA was added into 10 mL CB and stirred one night at 80 °C to obtain a transparent solution.

Growth of $MAPbBr_3$ microwire arrays (MWAs)

The silicon template with microwire patterns was first etched by inductively coupled plasma (ICP)[32,33]. PDMS and curing agent were mixed with a mass ratio of 10:1 to de-mold microwire patterns on the silicon template to obtain the PDMS mold with 20-μm width and 32-μm depth channels. Then the PDMS mold was aligned and bonded onto a pre-patterned indium tin oxide (ITO) glass substrate. 5 μL precursor solution was injected into the

PDMS channel inlets and capillary-driven to fill the entire channels. The substrate was then heated at 60 °C for 1 h to facilitate solvent evaporation and crystallization. After complete drying, the PDMS mold was gently peeled off, yielding uniform $MAPbBr_3$ MWAs at the ITO/glass boundary.

Synthesis of the $MAPbBr_3$-$MAPbBr_{3-x}I_x$ microwire heterostructure arrays

A 100-μm-diameter gold wire was vertically positioned atop the $MAPbBr_3$ MWAs to restrict the flow of PMMA solution. 50 μL PMMA solution (cooled to room temperature to avoid bubble formation) was drop-cast to fully cover the ITO side of the $MAPbBr_3$ MWAs. The gold wire was then gently removed, and the substrate was heated at 90 °C for 3 min to form a smooth and transparent PMMA film. For halide exchange, hydroiodic acid was vapor-phase diffused by placing 1 mL HI in a 10-mL glass vial within a 50-mL sealed beaker containing desiccant (silica gel). The PMMA-half-covered substrate was exposed to HI vapor at 48 °C for 15 h, followed by post-annealing at 60 °C for 15 min to obtain the $MAPbBr_3$-$MAPbBr_{3-x}I_x$ microwire heterostructure arrays.

Characterization of the microwire arrays

The morphologies were obtained by scanning electron microscopy (SEM, Sigma FE-SEM, Zeiss, Germany). The atomic force microscope (AFM) was supplied by Dimension Icon, Bruker, Germany. The optical images and fluorescent images were captured with a microscope from AxioCam ICC 5, Zeiss, Germany. The crystal structure was characterized by X-ray diffraction (XRD) from Smartlab, Rigaku, Japan, using a rotating anode X-ray source with Cu ($\lambda \sim 1.54$ Å) and 0.01° step. The absorption spectrum was obtained by a UV-vis/NIR spectrophotometer (UV-2600, Shimadzu, Japan). The PL spectra were obtained by a Confocal Laser Raman Spectrometer (LabRAM HR Evolution, Horiba, Japan) with a 325 nm excitation laser.

Photoelectronic testing of the PMH-SPD

The device configuration is ITO/$MAPbBr_3$/$MAPbBr_{3-x}I_x$/Au, with a 400-μm length and 3-mm width, which contains approximately 150 microwires. Therefore, the effective illuminated area is about 8.1×10^{-4} cm^2. The electrical characteristics (*I-V*, *I-T*) were measured by a semiconductor device analyzer (B1500A, Keysight, USA) equipped with a probe station (Semishare, China) and a silver probe. The excitation light sources of the device were the semiconductor lasers at 450 nm and 650 nm with maximum power intensities of 53.12 mW and 74.97 mW (light spot area of 0.49 cm^2), respectively. The laser power was regulated by an attenuator (FW1, Thorlabs, USA) and measured by a photodiode power sensor (S130VC, Thorlabs, USA). The response speed was measured with the mixed domain oscilloscope (MDO4054C, Tektronix, USA) cooperated with a low-noise current preamplifier (SR570, Stanford Research Systems, USA), and the optical switch of the laser source was controlled with a function/arbitrary waveform generator (DG4062, Rigol, China). The spectral response was measured using a response measurement system equipped with a monochromator (Zolix Instruments, China), a lock-in amplifier (SR830, Stanford Research Systems, USA), and a 150 W chopper-modulated xenon lamp; 450 nm illumination offered by an unmodulated semiconductor laser only generated a direct current (DC) signal, which was filtered by the lock-in amplifier. The spectrum distributions of the projector's light were measured by a miniature spectrometer (FLAME-T-VIS-NIR-ES, Ocean Insight, USA). All measurements were taken at room temperature in a nitrogen gas environment.

Imaging process

The imaging system is shown in Fig. 1. The color images were projected on the DMD (RAY_DDR065, Rayscience, China) by a projector (EP-970, Epson, Japan). Meanwhile, the DMD displayed a series of 32/64-order Hadamard patterns with a frame rate of 20 Hz. Then the PMH-SPD and a commercial silicon detector (PDA100A2, Thorlabs, USA) detected the reflected light from DMD through a scattering medium (a 100 μm thick laminating pouch film from Miracle company)[31]. A low-noise signal amplifier (SR570, Stanford Research Systems, USA) was further employed to collect the optical signals, then recorded by using a computer-hosted data acquisition card (PCIe-6251, NI, USA). The target image T was reconstructed by correlating the recorded signal b_i and the corresponding illumination patterns H_i (x, y) through the following differential correlation imaging algorithm:

$$T(x,y) = \frac{1}{M}\sum_{i=1}^{M} b_i H_i(x,y) - \frac{\overline{b}}{\overline{h}}\frac{1}{M}\sum_{i=1}^{M} h_i H_i(x,y) \quad (1)$$

where $\overline{b} = \frac{1}{M}\sum_{i=1}^{M} b_i$ represents the average value of the recorded signals. $M = 2048$ or 8192 represents the total number of 32- or 64-order Hadamard patterns. $\overline{h} = \frac{1}{M}\sum_{i=1}^{M} h_i$ represents the average total pixel values of M illumination patterns, in which the total pixel value of illumination pattern h_i is calculated by $h_i = \sum_{x=1}^{n}\sum_{y=1}^{n} H_i(x,y)$, $n = 32$ or 64.

Acknowledgements

We acknowledge support from the Science and Technology Development Fund from Macau SAR (FDCT) (0105/2023/RIA2, 0083/2023/ITP2, 0002/2024/TFP), the Multi-year Research Grants (MYRG-GRG2023-00230-IAPME-UMDF, MYRG-GRG2024-00069-IAPME) from the University of Macau, and Quantum Science Center of Guangdong-Hong Kong-Macau Great Bay Area (GDZX2204004, GDZX2304001).

Author details
[1]Institute of Applied Physics and Materials Engineering, University of Macau, Taipa, Macao SAR, China. [2]State Key Laboratory of High Power Semiconductor Lasers, Changchun University of Science and Technology, Changchun, China. [3]Department of Physics, Applied Optics Beijing Area Major Laboratory, Beijing Normal University, Beijing, China. [4]New Cornerstone Science Laboratory, Department of Physics, University of Hong Kong, Hong Kong, China. [5]Department of Electrical and Electronic Engineering, University of Hong Kong, Hong Kong, China

Author contributions
A.F., S.Z., S.-P.W. and H.-C.L. conceived the idea. A.F. and Z.-H.Z. conducted the device fabrication and characterization with contributions from Z.-P.W. A.F. performed the imaging experiments with contributions from J.H.X., X.Z., Z.Y.Y. and J.X. All authors contributed to the manuscript writing. All authors have approved the final version of the manuscript.

Data availability
The data presented in the manuscript is available from the corresponding author upon reasonable request.

Conflict of interest
Shuang Zhang is an Editor for the journal, and no other author has reported any competing interests.

Supplementary information The online version contains supplementary material available at https://doi.org/10.1038/s41377-025-02126-z.

Received: 20 May 2025 Revised: 30 October 2025 Accepted: 5 November 2025
Published online: 02 March 2026

References

1. Kaur, M. & Kumar, V. A comprehensive review on image encryption techniques. *Arch. Comput. Methods Eng.* **27**, 15–43 (2020).
2. SaberiKamarposhti, M., Ghorbani, A. & Yadollahi, M. A comprehensive survey on image encryption: taxonomy, challenges, and future directions. *Chaos Solitons Fractals* **178**, 114361 (2024).
3. Hou, J. F. & Situ, G. H. Image encryption using spatial nonlinear optics. *eLight* **2**, 3 (2022).
4. Chen, W., Javidi, B. & Chen, X. D. Advances in optical security systems. *Adv. Opt. Photonics* **6**, 120–155 (2014).
5. Matoba, O. et al. Optical techniques for information security. *Proc. IEEE* **97**, 1128–1148 (2009).
6. Fang, X. Y., Ren, H. R. & Gu, M. Orbital angular momentum holography for high-security encryption. *Nat. Photonics* **14**, 102–108 (2020).
7. Peng, D. M. et al. Optical coherence encryption with structured random light. *PhotoniX* **2**, 6 (2021).
8. Jiao, S. M. et al. Visual cryptography in single-pixel imaging. *Opt. Express* **28**, 7301–7313 (2020).
9. Liu, H. C. et al. Single-pixel computational ghost imaging with helicity-dependent metasurface hologram. *Sci. Adv.* **3**, e1701477 (2017).
10. Zheng, P. X. et al. Metasurface-based key for computational imaging encryption. *Sci. Adv.* **7**, eabg0363 (2021).
11. O'Toole, M., Lindell, D. B. & Wetzstein, G. Confocal non-line-of-sight imaging based on the light-cone transform. *Nature* **555**, 338–341 (2018).
12. Faccio, D., Velten, A. & Wetzstein, G. Non-line-of-sight imaging. *Nat. Rev. Phys.* **2**, 318–327 (2020).
13. Fossum, E. R. CMOS image sensors: electronic camera-on-a-chip. *IEEE Trans. Electron Devices* **44**, 1689–1698 (1997).
14. Shao, B. J. et al. Highly trustworthy in-sensor cryptography for image encryption and authentication. *ACS Nano* **17**, 10291–10299 (2023).
15. Shapiro, J. H. Computational ghost imaging. *Phys. Rev. A* **78**, 061802 (2008).
16. Gibson, G. M., Johnson, S. D. & Padgett, M. J. Single-pixel imaging 12 years on: a review. *Opt. Express* **28**, 28190–28208 (2020).
17. Wu, Z. J. et al. Dynamic 3D shape reconstruction under complex reflection and transmission conditions using multi-scale parallel single-pixel imaging. *Light Adv. Manuf.* **5**, 34 (2024).
18. Ma, J. Y. et al. Quantum imaging using spatially entangled photon pairs from a nonlinear metasurface. *eLight* **5**, 2 (2025).
19. Zhang, Z. B. et al. Secured single-pixel broadcast imaging. *Opt. Express* **26**, 14578–14591 (2018).
20. Edgar, M. P., Gibson, G. M. & Padgett, M. J. Principles and prospects for single-pixel imaging. *Nat. Photonics* **13**, 13–20 (2019).
21. Stantchev, R. I. et al. Real-time terahertz imaging with a single-pixel detector. *Nat. Commun.* **11**, 2535 (2020).
22. Liang, S. Y. et al. Multi-mode elastic full-color fluorescent patterns for multi-visual encryption. *Laser Photonics Rev.* **19**, 2400307 (2025).
23. Ghadirli, H. M., Nodehi, A. & Enayatifar, R. An overview of encryption algorithms in color images. *Signal Process.* **164**, 163–185 (2019).
24. Tanha, M., Kheradmand, R. & Ahmadi-Kandjani, S. Gray-scale and color optical encryption based on computational ghost imaging. *Appl. Phys. Lett.* **101**, 101108 (2012).
25. Filip, M. R. et al. Steric engineering of metal-halide perovskites with tunable optical band gaps. *Nat. Commun.* **5**, 5757 (2014).
26. Lim, J. et al. Long-range charge carrier mobility in metal halide perovskite thin-films and single crystals via transient photo-conductivity. *Nat. Commun.* **13**, 4201 (2022).
27. García de Arquer, F. P. et al. Solution-processed semiconductors for next-generation photodetectors. *Nat. Rev. Mater.* **2**, 16100 (2017).
28. Wu, W. Q. et al. Recent progress on wavelength-selective perovskite photodetectors for image sensing. *Small Methods* **7**, 2201499 (2023).
29. Zhao, Y. J. et al. Multifunctional perovskite photodetectors: from molecular-scale crystal structure design to micro/nano-scale morphology manipulation. *Nano Micro Lett.* **15**, 187 (2023).
30. Liu, Y. J. et al. Perovskite-based color camera inspired by human visual cells. *Light Sci. Appl.* **12**, 43 (2023).
31. Xiong, J. H. et al. Perovskite single-pixel detector for dual-color metasurface imaging recognition in complex environment. *Light Sci. Appl.* **12**, 286 (2023).
32. Zhang, Z. H. et al. Ultrasensitive perovskite photodetector for filter-free color single-pixel imaging. *Adv. Optical Mater.* **11**, 2201847 (2023).
33. Zhang, Z. H. et al. Air-stable self-driven UV photodetectors on controllable lead-free $CsCu_2I_3$ microwire arrays. *ACS Appl. Mater. Interfaces* **16**, 10398–10406 (2024).
34. Wang, M. et al. Flexible and self-powered lateral photodetector based on inorganic perovskite $CsPbI_3$-$CsPbBr_3$ heterojunction nanowire array. *Adv. Funct. Mater.* **30**, 1909771 (2020).
35. Li, S. X. et al. Flexible, self-powered, and polarization-sensitive photodetector based on perovskite lateral heterojunction microwire arrays. *Photonics Res.* **11**, 2231–2241 (2023).
36. Zhang, M. N. et al. Spectrum projection with a bandgap-gradient perovskite cell for colour perception. *Light Sci. Appl.* **9**, 162 (2020).
37. Kang, Y. B. et al. Ultrahigh-performance and broadband photodetector from visible to shortwave infrared band based on GaAsSb nanowires. *Chem. Eng. J.* **501**, 157392 (2024).
38. Kang, Y. B. et al. Enhanced visible-NIR dual-band performance of GaAs nanowire photodetectors through phase manipulation. *Adv. Optical Mater.* **13**, 2500289 (2025).
39. Ferri, F. et al. Differential ghost imaging. *Phys. Rev. Lett.* **104**, 253603 (2010).
40. Pratt, W. K., Kane, J. & Andrews, H. C. Hadamard transform image coding. *Proc. IEEE* **57**, 58–68 (1969).
41. Fang, L. J. et al. Deep learning-based point-scanning super-resolution imaging. *Nat. Methods* **18**, 406–416 (2021).
42. Funatomi, T. et al. Eliminating temporal illumination variations in whisk-broom hyperspectral imaging. *Int. J. Comput. Vis.* **130**, 1310–1324 (2022).
43. Sezgin, M. & Sankur, B. Survey over image thresholding techniques and quantitative performance evaluation. *J. Electron. Imaging* **13**, 146–165 (2004).
44. Chen, L. F. & Zhao, D. M. Optical color image encryption by wavelength multiplexing and lensless Fresnel transform holograms. *Opt. Express* **14**, 8552–8560 (2006).
45. Chen, W., Quan, C. & Tay, C. J. Optical color image encryption based on Arnold transform and interference method. *Opt. Commun.* **282**, 3680–3685 (2009).
46. Moseley, O. D. I. et al. Tunable multiband halide perovskite tandem photodetectors with switchable response. *ACS Photonics* **9**, 3958–3966 (2022).
47. Lin, Q. Q. et al. Filterless narrowband visible photodetectors. *Nat. Photonics* **9**, 687–694 (2015).
48. Fang, Y. J. et al. Highly narrowband perovskite single-crystal photodetectors enabled by surface-charge recombination. *Nat. Photonics* **9**, 679–686 (2015).
49. Li, J. Z. et al. Self-trapped state enabled filterless narrowband photodetections in 2D layered perovskite single crystals. *Nat. Commun.* **10**, 806 (2019).